2024 IEEE International Conference on Robotics and Automation (ICRA 2024)
May 13-17, 2024. Yokohama, Japan

A Generic Modeling Framework For the Design of Tendon-Driven Continuum Manipulators with Flexure Patterns

Yang Liu[1], Hansoul Kim[1], Yash Kulkarni[1], and Farshid Alambeigi[1]

***Abstract*— In this paper, a novel mathematical framework is introduced for modeling deformation behavior of Tendon-Driven Continuum Manipulators (TD-CMs) featuring discontinuous cross-sectional geometries (i.e., having flexural patterns). Leveraging this framework, we also introduce the concept of design space by which the deformation-behavior space of a TD-CM can intuitively be analyzed via its geometrical design parameters. To thoroughly evaluate the performance of the proposed modeling framework, we have conducted various simulation studies and experiments.**

I. Introduction

Tendon-driven continuum manipulators (TD-CMs) are soft robots that are designed to mimic the dexterity and flexibility of natural biological systems [1]. TD-CMs are highly versatile and adaptable, making them well-suited for a wide range of applications, such as minimally invasive surgeries (e.g., [2], [3]), where small incisions are made and the robot is inserted into the body. The flexibility and controllability of the TD-CM allows it to navigate through tight spaces and manipulate surgical instruments with precision [4]. While TD-CMs offer a lot of promise for various surgical applications, their modeling and design come with the following significant challenges. Firstly, due to their inherent compliance and highly nonlinear deformation, their mechanical properties are complex, which makes it challenging to accurately model and simulate their behavior [1], [4], [5], [6], [7].

Through the years, the literature has seen the emergence of diverse modeling approaches for TD-CMs [1]. For instance, Rucker et al. [8] formulated deformation behavior of TD-CMs using the Cosserat rod theory, featuring general tendon routing and external loading. Also, Renda et al. [9] introduced a model for the dynamics of multi-section TD-CMs using a discrete Cosserat approach. In summary, an examination of the literature indicates that the majority of existing approaches in modeling deformation behavior of TD-CMs– including both piecewise *constant-curvature* models (e.g., [10]) and *variable-curvature* models (e.g., [8]) often focus on modeling TD-CMs with a continuous circular cross sectional geometry. Recently, Chitalia et al. [11] designed a TD-CM incorporating flexure patterns and a partially-constrained tendon routing system to enhance its operational workspace. In another study, Pacheco et al. [12] introduced an innovative mechanics model rooted in Castigliano's second theorem. While the proposed approaches incorporate tip displacement modeling, they rely on a simplified beam model that is tailored to a specific design and lacks versatility for application to generic TD-CMs. Although studies have addressed TD-CMs with continuous circular cross sections, extending these established modeling methods to TD-CMs with discontinuous cross-section geometries (i.e., discrete flexural patterns) presents a considerable challenge. This challenge arises from the utilization of classic Cosserat rod differential equilibrium equations and boundary value problem (BVP) formulations [8] in these models. Such approaches may result in numerical instability, as observed in the context of these robots [13].

To overcome the above-mentioned constraints and as the primary contributions of this investigation: (1) We present a novel modeling framework grounded in Cosserat rod theory and tailored for TD-CMs with intermittent cross-section geometries featuring discrete flexural patterns. In contrast to earlier research, the suggested modeling framework is capable of accommodating a generic discontinuous cross-section geometries, enabling the design and incorporation of discrete flexural patterns to enhance the TD-CM's flexibility and steerability; (2) We propose a novel solution algorithm that is specifically designed for this type of TD-CM structure. Contrary to existing algorithms, our algorithm eliminates the need to solve the conventional Cosserat rod differential equilibrium equation and its boundary value problem formulation. This is particularly advantageous for TD-CMs with discontinuous geometries, which can lead to numerical stability issues; (3) We also introduce the concept of "design space" that effectively illustrates the relationship between the TD-CM's deformability, geometric design variables, and tendon actuation force. This distinctive feature can streamline the process of designing and, most notably, fine-tuning the steering capabilities of robotic TD-CMs; and (4) To evaluate and analyze the effectiveness of the proposed design framework in predicting deformation behavior of TD-CMs with discrete flexural patterns, we designed and fabricated a novel TD-CM actuation system and used Vicon motion capture system (Vero, Vicon Motion Systems, Ltd.) to evaluate the proposed model.

II. Mathematical Modeling

To provide an effective tool for modeling and incorporating discrete flexural patterns for enhancing the TD-CM's flexibility and steerability, and to better understand the deformation behavior of the TD-CM and predict its performance,

*Research reported in this publication was supported by the National Institute of Biomedical Imaging and Bioengineering of the National Institutes of Health under Award Number R21EB030796.

[1]Y. Liu, H. Kim, Y. Kulkarni, and F. Alambeigi are with the Walker Department of Mechanical Engineering and and the Texas Robotics at the University of Texas at Austin, Austin, TX, 78712. (Email: {liu.yang, kulkarni.yash08}@utexas.edu, {han.kim, farshid.alambeigi}@austin.utexas.edu).

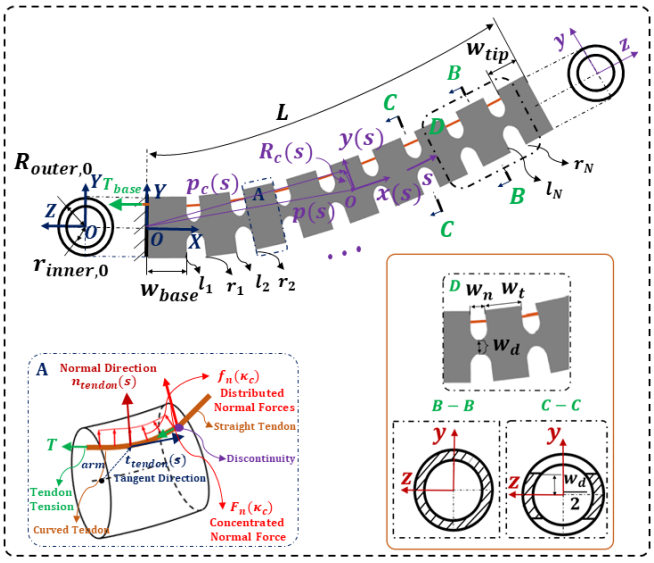

Fig. 1. Conceptual illustration of a TD-CM with flexure patterns.

we propose a new mathematical modeling framework. This modeling framework is specifically designed to handle TD-CMs with discontinuous cross-section geometries (i.e., with discrete flexural patterns).

Remark 1: As shown in Fig.1, for a TD-CM with discontinuous cross-section geometries, the tendon is partially constrained inside its channel. Due to the discontinuity of both geometry and tendon routing, the modeling framework proposed for a TD-CM with continuous geometry (e.g., [4], [7], [1], [8]) cannot directly be applied to this case.

Remark 2: Our proposed modeling framework for TD-CMs with discrete flexural patterns utilizes a novel iterative algorithm specifically designed for this type of structure. Unlike existing algorithms such as the shooting method [14], our algorithm eliminates the need to solve the conventional Cosserat rod differential equilibrium equation and its boundary value problem formulation [8]. This is particularly advantageous for TD-CMs with flexural patterns, as their second moment of area cross section functions may not be differentiable, leading to numerical stability issues [8].

A. TD-CM Geometry

As shown in Fig. 1, let's consider a generic TD-CM that utilizes a flexure pattern that includes N evenly and symmetrically distributed notches on each side of the robot body. As a result, the overall length of the TD-CM can be expressed as: $L = w_{base} + N \cdot w_n + (N-1) \cdot w_t + w_{tip}$ In this context, w_{base} and w_{tip} refer to the lengths of the proximal and distal segments of the TD-CM. w_n indicates the width of each notch, and w_t indicates the distance between two adjacent notches. The width of the TD-CM's backbone is denoted by w_d. Importantly, customization and tailoring of the TD-CM's flexibility and steerability to meet specific application requirements can be achieved by adjusting these design parameters.

For such a manipulator, l_i is defined as the length of the left segment up to the i-th notch, and r_i is defined as the length of the right segment up to the i-th notch, as shown in Fig. 1. With this definition, the values of l_i and r_i are dependent on the parameters w_{base}, w_n, w_t, and N and can be defined as follows:

$$\begin{cases} l_i = w_{base} + (i-1) \cdot w_n + (i-1) \cdot w_t \\ r_i = w_{base} + i \cdot w_n + (i-1) \cdot w_t \end{cases} \tag{1}$$

where $i \in [1, N]$ is an integer.

B. TD-CM Kinematics

As illustrated in Fig. 1 and in alignment with the provided reference frames, we elucidate the planar deformation characteristics of the TD-CM featuring discontinuous cross-section geometries (specifically, discrete flexural patterns). This description is based on the body frame pose along the midline arc length parameter $s \in [0, L]$, with reference to the global frame XYZ. The homogeneous transformation matrix $T(s) \in SE(3)$ is then used to represent the transformation from the body frame $\{xyz\}$ to the global frame $\{XYZ\}$. In this context, L is the total length of the TD-CM's midline, $\boldsymbol{p}(s) \in \mathbb{R}^3$ indicates the position vector, and $\mathcal{R}(s) = [\boldsymbol{x}(s),\ \boldsymbol{y}(s),\ \boldsymbol{z}(s)] \in SO(3)$ denotes the orientation matrix for the body frame xyz [5], [6], [13]. The progressive transformation of the body frame configuration along the arc length parameter s is elucidated through the twist vector $V_b(s) = [\omega_b(s), v_b(s)]^T \in \mathbb{R}^6$. This vector encapsulates the angular and linear rates of change of the configuration $T(s)$ concerning s. The derivative of $T(s)$ with respect to s (i.e., $T'(s)$) is expressed as follows:

$$T'(s) = \begin{pmatrix} \mathcal{R}(s) & \boldsymbol{p}(s) \\ \mathbf{0}^T & 1 \end{pmatrix} \begin{pmatrix} [\omega_b(s)] & v_b(s) \\ \mathbf{0}^T & 0 \end{pmatrix} \tag{2}$$

In this context, $v_b(s) \in \mathbb{R}^3$ signifies the linear rate of change, and $[\omega_b(s)] \in so(3)$ represents the skew-symmetric matrix form of the angular rate of change, $\omega_b(s) \in \mathbb{R}^3$. The symbol " $'$ " denotes the derivative with respect to s in all instances within this paper.

C. Kinematics of Tendon

As shown in the zoomed region A of Fig. 1, in this section, we will derive the kinematics of a tendon to accurately model the internal forces that are distributed along the tendon channel and concentrated at the discontinuous points where the tubular section meets the notched section.

Unlike the cases in which the tendon is fully constrained in TD-CMs (e.g., [4]), the tangent direction of a tendon curve $\boldsymbol{p}_c(s)$ that is partially constrained in TD-CM with discrete flexural patterns can be described as follows:

$$\boldsymbol{t}_{\text{tendon}}(s) = \begin{cases} \dfrac{\boldsymbol{p}_c'(s)}{\|\boldsymbol{p}_c'(s)\|} & s \in (l_i, r_i) \\ \dfrac{\boldsymbol{p}_c(l_{i+1}) - \boldsymbol{p}_c(r_i)}{\|\boldsymbol{p}_c(l_{i+1}) - \boldsymbol{p}_c(r_i)\|} & otherwise \end{cases} \tag{3}$$

Here, the position vector $\boldsymbol{p}_c(s)$ can be expressed as follows:

$$\boldsymbol{p}_c(s) = \begin{cases} \boldsymbol{p}(s) + \boldsymbol{R}_c(s) & s \in (l_i, r_i) \\ \boldsymbol{p}_c(r_i) + \dfrac{(\boldsymbol{p}_c(l_{i+1}) - \boldsymbol{p}_c(r_i))(s - r_i)}{l_{i+1} - r_i} & otherwise \end{cases} \tag{4}$$

The position vector of TD-CM's midline is denoted by $\boldsymbol{p}(s)$, while a vector from the origin of the body frame $\{xyz\}$ to the corresponding point on the tendon is denoted by $\boldsymbol{R}_c(s)$. Using the Frenet–Serret Formulas [4], tendon curvature can be expressed as:

$$\kappa_c(s) = \begin{cases} \dfrac{\|\boldsymbol{p}_c'(s) \times \boldsymbol{p}_c''(s)\|}{\|\boldsymbol{p}_c'(s)\|^3} & s \in (l_i, r_i) \\ 0 & otherwise \end{cases} \tag{5}$$

It is also possible to obtain the normal direction of tendon curvature, denoted by $\boldsymbol{n}_{\text{tendon}}$:

$$\boldsymbol{n}_{\text{tendon}}(s) = \begin{cases} \dfrac{\boldsymbol{p}_c'(s) \times (\boldsymbol{p}_c''(s) \times \boldsymbol{p}_c'(s))}{\|\boldsymbol{p}_c''(s) \times \boldsymbol{p}_c'(s)\| \cdot \|\boldsymbol{p}_c'(s)\|} & s \in (l_i, r_i) \\ 0 & otherwise \end{cases} \tag{6}$$

D. Internal Forces along a Tendon

Tendon tension $\boldsymbol{T}(s)$ as a function of the arc length parameter s can be written as [4]: $\boldsymbol{T}(s) = -\boldsymbol{t}_{\text{tendon}}(s) \cdot T_{\text{base}}$. where T_{base} is the input tendon tension. As shown in the zoomed region A of Fig. 1, distributed normal forces along the tendon channel can be expressed as [4]: $\boldsymbol{f}_n(\kappa_c) = \boldsymbol{n}_{\text{tendon}}(s) \cdot \kappa_c(s) \cdot T_{\text{base}}$. Due to the presence of discontinuous points where the tubular section meets the notched section, it is necessary to take into account concentrated point forces at these locations during the modeling process. To model these forces, the change in angle θ in the tangent direction of the tendon curve at these discontinuous points can be expressed as follows:

$$\theta = \begin{cases} \sin^{-1} \dfrac{\boldsymbol{t}_{\text{tendon}}(l_i^-) \times \boldsymbol{t}_{\text{tendon}}(l_i^+)}{|\boldsymbol{t}_{\text{tendon}}(l_i^-) \cdot \boldsymbol{t}_{\text{tendon}}(l_i^+)|} & s = l_i \\ \sin^{-1} \dfrac{\boldsymbol{t}_{\text{tendon}}(r_i^-) \times \boldsymbol{t}_{\text{tendon}}(r_i^+)}{|\boldsymbol{t}_{\text{tendon}}(r_i^-) \cdot \boldsymbol{t}_{\text{tendon}}(r_i^+)|} & s = r_i \end{cases} \tag{7}$$

In the above equations, the symbol "$-$" is used when s approaches l_i and r_i from the left, while the symbol "$+$" is used when s approaches l_i and r_i from the right. Using equation (7), the concentrated point forces can be written as: $\boldsymbol{F}_n(\kappa_c) = \boldsymbol{n}_{\text{tendon}}(s) \cdot T_{\text{base}} \cdot \sin\theta$.

E. Distributed Moment on the TD-CM's Midline

The total moment $\boldsymbol{m}_{total}$ exerted by the tendon on the TD-CM's midline is composed of the contribution of the anchor point force, distributed normal forces along the tendon channel, and concentrated point forces. The moment $\boldsymbol{m}_a$ generated by the anchor point force is calculated as the cross product of the arm vector and the anchor point force vector:

$$\boldsymbol{m}_a(s) = \underbrace{(\boldsymbol{p}_c(L) - \boldsymbol{p}(s))}_{arm} \times \underbrace{(-\boldsymbol{t}_{\text{tendon}}(L) \cdot T_{\text{base}})}_{anchor\ point\ force} \tag{8}$$

To express the moment $\boldsymbol{m}_n$ resulting from the distributed normal forces, one can integrate the cross product of the arm vector and the distributed normal forces, which can be represented as:

$$\boldsymbol{m}_n(s) = \int_s^L \underbrace{(\boldsymbol{p}_c(\xi) - \boldsymbol{p}(s))}_{arm} \times \underbrace{\boldsymbol{f}_n(\kappa_c)}_{distributed\ normal\ forces} d\xi \tag{9}$$

The moment $\boldsymbol{m}_n$ produced by the concentrated point forces is obtained by taking the cross product of the arm vector and the concentrated point force vector:

$$\boldsymbol{m}_{cn}(s) = \sum_{\xi = l_i, r_i}^{l_N, r_N} \underbrace{(\boldsymbol{p}_c(\xi) - \boldsymbol{p}(s))}_{arm} \times \underbrace{\boldsymbol{F}_n(\kappa_c)}_{concentrated\ point\ force} \tag{10}$$

Therefore, the total moment $\boldsymbol{m}_{total}$ exerted by the tendon on the TD-CM's midline can be expressed as:

$$\boldsymbol{m}_{total}(s) = \boldsymbol{m}_a(s) + \boldsymbol{m}_{cn}(s) + \boldsymbol{m}_n(s) \tag{11}$$

F. Geometric Modeling of TD-CM

The proposed TD-CM exhibits discontinuous cross-sectional geometries, in contrast to the TD-CM (e.g., [4]) that has a continuous geometry. As a result, the second moment of area $I_z(s)$ of the TD-CM's cross sections about the z axis can be expressed using the following piecewise function:

$$I_z(s) = \begin{cases} 4[\displaystyle\int_0^{h_1(s)} (R_{outer,0}^2 - y^2)^{\frac{1}{2}} y^2 dy - \\ \displaystyle\int_0^{h_2(s)} (r_{inner,0}^2 - y^2)^{\frac{1}{2}} y^2 dy] & s \in (l_i, r_i) \\ \dfrac{\pi}{4}(R_{outer,0}^4 - r_{inner,0}^4) & otherwise \end{cases} \tag{12}$$

where

$$\begin{cases} h_1(s) = \frac{w_n + w_d}{2} + |\sin t| \cdot \frac{w_n}{2} \cdot sign(\sin t) \\ h_2(s) = \begin{cases} \frac{w_n + w_d}{2} + |\sin t| \cdot \frac{w_n}{2} \cdot sign(\sin t) \\ r_{inner,0} \quad if \ \ h_2 > r_{inner,0} \end{cases} \end{cases} \tag{13}$$

G. Equilibrium Equation

In our previous work [13], we highlighted the widespread use of the classical form of the Cosserat rod differential equilibrium equation [5] in modeling continuum manipulators [8]. For the specific TD-CM considered in this study with a varying cross-sectional geometry, the stiffness matrix $\boldsymbol{K}_w(s)$ can be defined as $\boldsymbol{K}_w(s) = EI_z(s)$, where E is the Young's modulus and $I_z(s)$ is the piecewise second moment of area function. However, modeling TD-CM with discontinuous cross-sectional geometries (i.e., with discrete flexural patterns) using the classical form of the Cosserat rod theory leads to numerical stability issues due to the non-differentiability of the piecewise second moment of area functions. This is because the classical form requires taking the derivative of $\boldsymbol{K}_\omega$ with respect to s to model TD-CMs

Algorithm 1: Solution Algorithm

Input: T_{base};
Initialization:
$I_z \longleftarrow$ Calculate the second moment of area (12);
$k \longleftarrow 0$;
Iterative Process:
do
  $\boldsymbol{m}_{total}^{k+1} \longleftarrow$ Calculate total moment exerted by the tendon (11);
  $\omega_b^{k+1} \longleftarrow$ Solve equilibrium equation (14);
  $T^{k+1} \longleftarrow$ Solve ODE equation (2);
  $[\boldsymbol{p}^{k+1}, \mathcal{R}^{k+1}] \longleftarrow$ Find position vector and orientation matrix (2);
  $k \longleftarrow k+1$;
while $\|\boldsymbol{p}^{k+1}(s) - \boldsymbol{p}^{k}(s)\| > \epsilon$;
Output: $\boldsymbol{p}$, $\mathcal{R}$

with varying cross sections, which involves differentiating $I_z(s)$ on the boundary.

To overcome the numerical stability issues in modeling TD-CMs with discontinuous cross-sectional geometries, we have developed new formulations and a solution algorithm (i.e., Algorithm 1). Specifically, we consider a TD-CM, as depicted in Fig.1, and express the relationship between the total moment $\boldsymbol{m}_{total}(s)$ exerted by the tendon and the deformation behavior of the TD-CM using equations (11) and (12). We then apply the static equilibrium equation:

$$\boldsymbol{m}_{total}(s) = \boldsymbol{K}_w(s) \cdot \omega_b(s) \tag{14}$$

It is important to mention that the iteration process stops when the difference between the TD-CM's positions calculated in two consecutive iterations is lower than a predetermined threshold value ϵ. As previously mentioned, the proposed modeling framework is not specific to TD-CMs with a particular flexural pattern geometry. Instead, it can be applied to TD-CMs with various flexural pattern geometries by updating the stiffness matrix $\boldsymbol{K}_w(s)$.

III. Evaluation

A. Simulation Studies

To assess the performance of our proposed modeling framework and solution algorithm, we conducted simulations using MATLAB (MathWorks, Inc.). These simulations involved varying geometric parameters, specifically the notch width (w_n) and backbone width (w_d), which aimed to explore the effects of three distinct scenarios for each geometric parameter (i.e., notch width and backbone width) on TD-CMs' bending performance. Moreover, both simulations utilized TD-CMs with identical design parameters, as outlined in Fig. 1: $L = 53$ mm, $w_{base} = 5$ mm, $N = 8$, $R_{outer,0} = 3.92$ mm, $r_{inner,0} = 1.55$ mm. To maintain a consistent overall TD-CM length, we set: $w_t = 6\text{-}w_n$, $w_{tip} = w_t$. It's important to emphasize that our proposed modeling framework is generic and adaptable to different applications, allowing for the adjustment of parameters as needed for specific use cases. In Fig. 2(a) and Fig. 3(a), we compare the deformation characteristics of the three distinct scenarios, encompassing various notch widths (i.e., $w_n = 1, 1.9$, and 2.5 mm) and backbone widths (i.e., $w_d = 1.2, 1.52$, and 2 mm). These comparisons were conducted under an arbitrarily chosen input tendon tension of $T_{\text{base}} = 20$ N. Fig. 2(b) and Fig. 3(b) depict the distribution of curvature along the midline of TD-CMs. In Fig. 2(c) and Fig. 3(c), we present the "*design space*" and provide a contrast with the "*design curves*." The "*design space*" is generated by our proposed model, showcasing the entire range of geometric parameters (notch widths (w_n) and backbone widths (w_d) and tip displacements (d) as the input tension varies from $T_{\text{base}} = 0$ to 20 N.

B. Experimental Studies

To evaluate the framework's performance in predicting the deformation behavior of TD-CMs with flexural patterns, we designed and fabricated a compact and lightweight TD-CM actuation system and used Vicon motion capture system to measure the robot's shape. As depicted in Fig. 4(a), the proposed robotic system includes a TD-CM with flexure patterns and a unique actuation unit for bending the manipulator. The TD-CM is fabricated using elastic and durable Nylon 12 Powder (Formlabs) with SLS printing. Its geometry is defined by the parameters presented in Fig. 1, namely: $L = 53$ mm, $R_{\text{outer},0} = 3.92$ mm, $r_{\text{outer},0} = 1.55$ mm, $w_{base} = 5$ mm, $w_{tip} = 4$ mm, $w_n = 2$ mm, $w_t = 4$ mm, $w_d = 1.4$ mm, $R_c(s) = 2.75$ mm and $N = 8$. Actuation (bending the manipulator) is achieved by pulling a low-stretch coated wire rope (34235T26, McMaster-Car) with a diameter of 0.03 inch. In order to generate a specific tendon tension as an input, a load cell (LCM100, FUTEK Advanced Sensor Technology, Inc.) was employed to connect one end of the aforementioned wire rope to a linear actuator (HLS12-30100-6V, ServoCity). A servo gearbox (3216-0001-0009, ServoCity) was employed to produce a rolling motion for the TD-CM, providing sufficient degrees of freedom for TD-CMs to execute maneuvers for future implementations.

To capture the motion/deformation behavior of the TD-CM, Vicon motion capture system (Vero, Vicon Motion Systems, Ltd.) with five cameras was set around the experimental setup and a calibration part with three optical markers was utilized to define the coordinate frame visually in the Vicon NEXUS software, as shown in Fig. 4(b). As shown in Fig. 4(b), in this study, three reflective optical markers with 1 mm radius were attached to the TD-CM each located 15 mm, 33 mm and 53 mm from the base cross section to a cross section on which the markers were attached. To generate deformation behavior for the proposed TD-CM, input tension ($T_{\text{base}} = 0 \sim 20$ N with 4 N increments) was sent as a commend from the controller board (Arduino UNO) to the linear actuator (HLS12-30100-6V, ServoCity). The load cell (LCM100, FUTEK Advanced Sensor Technology, Inc.) was employed to provide tendon tension feedback signal to close the control loop. Of note, since the captured motion data of the TD-CM shape provides discrete locations of the optical markers, cubic spline data interpolation technique (*fit* function in MATLAB) was utilized to interpolate these

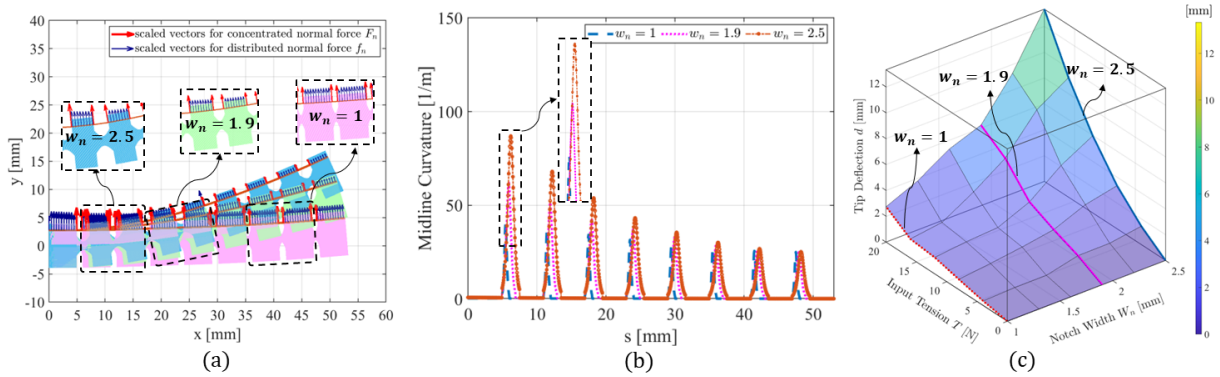

Fig. 2. Simulation results of TD-CMs with three different notch widths (i.e., $w_n = 1, 1.9$ and 2.5 mm) with an identical backbone width $w_d = 1.5$ mm: (a) Comparison and illustration of the TD-CMs' deformation behaviors with an identical input tension $T_{\text{base}} = 20$ N; (b) Comparison of the TD-CMs' midline curvatures along s with an identical input tension $T_{\text{base}} = 20$ N; (c) The surface represents the "*design space*" of all possible notch width w_n, and tip displacement d when the input tension is changing from $T_{\text{base}} = 0 \sim 20$ N. "*design curves*" (i.e., the curves labeled by $w_n = 1, 1.9$ and 2.5) represent the aforementioned relationship generated by specifying the notch width w_n and Fig. 1.

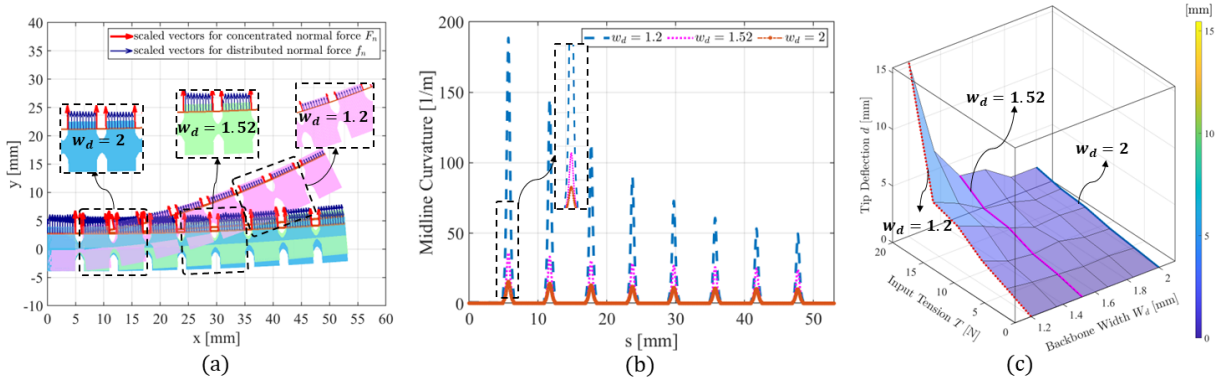

Fig. 3. Simulation results of TD-CMs with three different backbone widths (i.e., $w_d = 1.2, 1.52$ and 2 mm) with an identical notch width $w_n = 1.5$ mm: (a) Comparison and illustration of the TD-CMs' deformation behaviors with an identical input tension $T_{\text{base}} = 20$ N; (b) Comparison of the TD-CMs' midline curvatures along s with an identical input tension $T_{\text{base}} = 20$ N; (c) The surface represents the "*design space*" of all possible backbone width w_d, and tip displacement d when the input tension is changing from $T_{\text{base}} = 0 \sim 20$ N. "*design curves*" (i.e., the curves labeled by $w_d = 1.2, 1.52$ and 2) represent the aforementioned relationship generated by specifying the backbone width w_d and Fig. 1.

discrete points and create a smooth curve to represent the TD-CM's midline shape.

IV. Results and Discussion

In Fig. 2(a) and Fig. 2(b), we observe distinct deformation behaviors and midline curvature distributions despite using the same input tendon tension for the three analyzed flexural geometries (i.e., $w_n = 1, 1.9$, and 2.5 mm). These differences clearly illustrate the significant impact of these flexure geometries on the performance of a TD-CM. For instance, as depicted in Fig. 2(a), when we increase the notch width w_n from 1 mm to 2.5 mm, the TD-CM's maximum deformation increases. Conversely, when we increase the backbone width w_d from 1.2 mm to 2 mm, the TD-CM's maximum deformation decreases, as shown in Fig. 3(a) and Fig. 3(b). This underscores the crucial role of employing the proposed modeling approach as a design tool prior to the fabrication process. Furthermore, as illustrated in Fig. 2(c) and Fig. 3(c), even though the six selected geometries (comprising three different notch widths and three different backbone widths) are distinct, their corresponding "*design curves*" all reside within their respective "*design space*" and constitute a subset of the design space. It's important to highlight that for TD-CMs featuring discontinuous cross-sectional geometries or flexure patterns, their deformation characteristics, flexibility or steerability can be tuned by adjusting geometric parameters to meet the specific requirements of particular applications.

Fig. 4(c) shows a comparison between the experimental results and the model prediction for the TD-CM's midline shape. Of note, in this figure, the magenta circles indicate the locations of optical markers attached to the TD-CM's body, while the blue curve corresponds to the aforementioned cubic spline interpolation. As shown in TABLE I, the mean absolute percentage error (MAPE) of 2.51%, root mean square error (RMSE) of 0.54 mm, and mean absolute error (MAE) of 0.41 mm were used to measure the accuracy of the maximum tip deflection of the TD-CM in three repeated trials between experimental results and model predictions. *Shape_Error* of 0.85 mm is used to represent the deviation of the entire TD-CM's shape in three repeated trials between experimental results and model predictions. *Deflection_Mean* of 16.15 mm is the average value of the maximum tip deflection in three repeated experimental trials. Despite the discontinuous cross-section geometries (i.e., discrete flexural patterns) of the proposed TD-CM, the proposed model reliably and accurately obtained the robot's deformation behavior in three repeated trials. The prediction errors, including

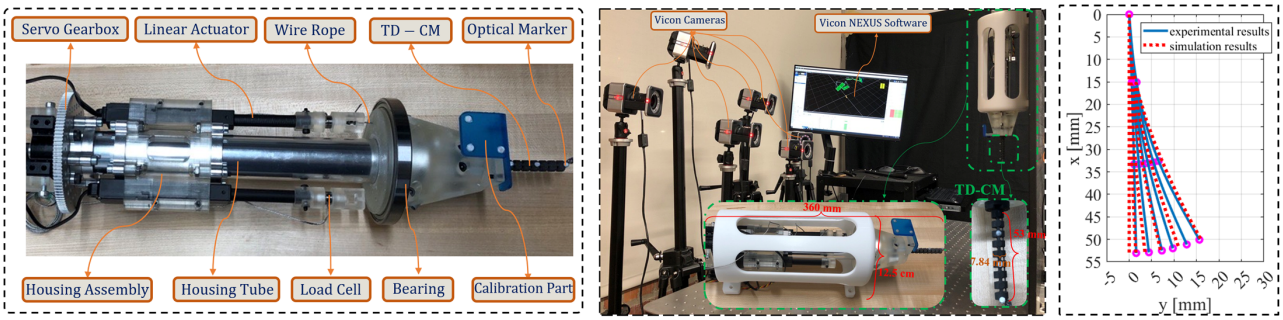

(a) (b) (c)

Fig. 4. (a) Main components of he proposed robotic system includes a TD-CM with flexure patterns and a unique actuation unit for bending the manipulator. (b) Overview of the experimental setup mainly comprising of a designed TD-CM and Vicon motion capture system. (c) Comparison of the proposed TD-CM's midline shape between the experimental results and model prediction with input tendon tension $T_{\text{base}} = 0 \sim 20$ N with a 4 N increment.

TABLE I

EXPERIMENTAL RESULTS FOR THE MAXIMUM TD-CM'S DEFLECTION IN THREE REPEATED TRIALS

Items	MAPE	RMSE	MAE	Shape_Error	Deflection_Mean
	2.51%	0.54 mm	0.41 mm	0.85 mm	16.15 mm

MAPE $< 3\%$, MAE/RMSE < 0.6 mm, and *Shape_Error* $<$ 0.9 mm, validated the accuracy of the proposed model and solution algorithm for modeling TD-CMs with discontinuous cross-section geometries. Importantly, our solution algorithm does not require solving the classic Cosserat rod differential equilibrium equation and its boundary value problem formulation [8], which is particularly advantageous for TD-CMs with flexural patterns because their second moment of area cross-section functions may not be differentiable, leading to numerical stability issues [8]. However, it's worth noting that discrepancies between the prediction and experimental results may be partly due to factors such as the SLS printing procedure of TD-CMs, frictional effects in tendon-tension transmission, measurement uncertainties, and/or inaccuracies in the Young's modulus used in the modeling.

V. CONCLUSION

This study introduces an analytical approach for modeling TD-CMs with discrete flexural patterns, utilizing a unique solution algorithm based on Cosserat rod theory. The algorithm eliminates the need for solving the classic Cosserat rod differential equilibrium equation, addressing numerical stability issues. The modeling framework provides a valuable "design space" to fine-tune steering capabilities by illustrating the interplay between TD-CM deformability, geometric design parameters, and tendon actuation forces. Simulations and experiments with varying geometric parameters validated the proposed framework's accuracy in predicting TD-CM deformation behavior. Future work includes extending the model to account for tension loss due to friction and applying the framework to design a TD-CM for steerable drilling of hard tissue [15].

REFERENCES

[1] P. E. Dupont, N. Simaan, H. Choset, and C. Rucker, "Continuum robots for medical interventions," *Proceedings of the IEEE*, vol. 110, no. 7, pp. 847–870, 2022.

[2] F. Alambeigi, M. Bakhtiarinejad, S. Sefati, R. Hegeman, I. Iordachita, H. Khanuja, and M. Armand, "On the use of a continuum manipulator and a bendable medical screw for minimally invasive interventions in orthopedic surgery," *IEEE Transactions on Medical Robotics and Bionics*, vol. 1, no. 1, pp. 14–21, 2019.

[3] F. Alambeigi, Y. Wang, S. Sefati, C. Gao, R. J. Murphy, I. Iordachita, R. H. Taylor, H. Khanuja, and M. Armand, "A curved-drilling approach in core decompression of the femoral head osteonecrosis using a continuum manipulator," *IEEE Robotics and Automation Letters*, vol. 2, no. 3, pp. 1480–1487, 2017.

[4] Y. Liu and F. Alambeigi, "Impact of generic tendon routing on tension loss of tendon-driven continuum manipulators with planar deformation," *IEEE Robotics and Automation Letters*, vol. 7, no. 2, pp. 3624–3631, 2022.

[5] Y. Liu, U. Yoo, S. Ha, S. F. Atashzar, and F. Alambeigi, "Influence of antagonistic tensions on distributed friction forces of multisegment tendon-driven continuum manipulators with irregular geometry," *IEEE/ASME Transactions on Mechatronics*, 2021.

[6] Y. Liu and F. Alambeigi, "Effect of external and internal loads on tension loss of tendon-driven continuum manipulators," *IEEE Robotics and Automation Letters*, vol. 6, no. 2, pp. 1606–1613, 2021.

[7] Y. Liu, S. Ahn, U. Yoo, A. Cohen, and F. Alambeigi, "Toward analytical modeling and evaluation of curvature-dependent distributed friction force in tendon-driven continuum manipulators," in *2020 IEEE/RSJ International Conference on Intelligent Robots and Systems (IROS), Las Vegas, NV, USA*, pp. 8823–8828, 2020.

[8] D. C. Rucker and R. J. Webster III, "Statics and dynamics of continuum robots with general tendon routing and external loading," *IEEE Transactions on Robotics*, vol. 27, no. 6, pp. 1033–1044, 2011.

[9] F. Renda, F. Boyer, J. Dias, and L. Seneviratne, "Discrete cosserat approach for multisection soft manipulator dynamics," *IEEE Transactions on Robotics*, vol. 34, no. 6, pp. 1518–1533, 2018.

[10] E. Tatlicioglu, I. D. Walker, and D. M. Dawson, "New dynamic models for planar extensible continuum robot manipulators," in *2007 IEEE/RSJ International Conference on Intelligent Robots and Systems*, pp. 1485–1490, IEEE, 2007.

[11] Y. Chitalia, S. Jeong, N. Deaton, J. J. Chern, and J. P. Desai, "Design and kinematics analysis of a robotic pediatric neuroendoscope tool body," *IEEE/ASME Transactions on Mechatronics*, vol. 25, no. 2, pp. 985–995, 2020.

[12] N. E. Pacheco, J. B. Gafford, M. A. Atalla, R. J. Webster III, and L. Fichera, "Beyond constant curvature: A new mechanics model for unidirectional notched-tube continuum wrists," *Journal of Medical Robotics Research*, vol. 6, no. 01n02, p. 2140004, 2021.

[13] Y. Liu, T. G. Mohanraj, M. R. Rajebi, L. Zhou, and F. Alambeigi, "Multiphysical analytical modeling and design of a magnetically steerable robotic catheter for treatment of peripheral artery disease," *IEEE/ASME Transactions on Mechatronics*, vol. 27, no. 4, pp. 1873–1881, 2022.

[14] C. B. Black, J. Till, and D. C. Rucker, "Parallel continuum robots: Modeling, analysis, and actuation-based force sensing," *IEEE Transactions on Robotics*, vol. 34, no. 1, pp. 29–47, 2017.

[15] S. Sharma, T. G. Mohanraj, J. P. Amadio, M. Khadem, and F. Alambeigi, "A concentric tube steerable drilling robot for minimally invasive spinal fixation of osteoporotic vertebrae," *IEEE Transactions on Biomedical Engineering*, pp. 1–11, 2023.